Exploiting amplitude of terrestrial radar data for feature tracking in areal monitoring of inhomogeneous surfaces

S. Conzett, A. Wieser, J. Butt
Institute of Geodesy and Photogrammetry,
ETH Zurich, Stefano-Franscini-Platz 5, 8093 Zurich, Switzerland

Abstract. The interferometric phase obtained from terrestrial radar data allows measuring the line-of-sight deformation component of surfaces discretized in azimuth-range bins. The amplitude information representing the strength of the backscattered signals is typically used for quality assessment of the phase. However, it can also be used to directly obtain information about the deformation process by tracking features in the temporal sequence of radar images as they travel through azimuth-range bins. Their trajectories provide valuable complementary information in cases where interferometry fails, e.g. due to loss of temporal coherence. Furthermore, this approach can potentially yield 2D displacement information (in range and azimuth) using images from a single radar instrument.

We present two approaches for amplitude feature tracking of natural surfaces within radar image sequences, one based on least squares template matching (LSM) and one on optical flow (OF). Spatial and temporal corrections are applied to increase the initially poor signal-to-noise ratio by mitigating atmospheric and material dependent effects.

The resulting algorithms are demonstrated using one month of data from the continuous monitoring of an alpine glacier (Bisgletscher/CH) with a radar interferometer from a distance of up to 6.5 km. Clusters of crevasses causing spatial variations of the amplitude were successfully tracked over the entire monitoring period. While LSM has particular potential for delivering accurate pointwise displacement information (without using artificial reflectors), OF is better suited for tracking spatially smooth deformation fields.

Keywords. Feature tracking, ground based radar interferometry, GPRI, radar amplitude, radar intensity, least squares template matching, optical flow, glacier monitoring

1 Introduction

Terrestrial radar interferometry (TRI) facilitates highly precise areal deformation monitoring based on the measured phase. Applications range from natural hazards monitoring (e.g. landslides, rock falls, glaciers) to low- and high-frequency structural monitoring (e.g. bridges, buildings, dams). The interferometric measurements yield estimates of the average displacements along the line-of-sight (LOS) associated with the respective range and azimuth bins of the radar images. The amplitude information, i.e. the strength of the backscattered signals, plays a minor role within the interferometric data processing. It is typically used for quality assessment of the phase, and – if needed – for image registration via cross-correlation (Hanssen, 2002).

However, information about deformation processes can also be obtained directly from the amplitude by tracking features which travel through the azimuth-range bins. This technique is especially suited for situations where interferometry fails, e.g. due to temporal decorrelation driven by the deformation process, changes of atmospheric conditions and changes of material properties of the scatterers.

Approaches based on normalized cross correlation have been tested for space-borne SAR applications commonly operating in the L-, C- and X-band. Strozzi et al. (2002) have applied this technique to natural scatterers of a glacier, Bhattacharya et al. (2014) to a landslide. Tracking artificial corner cube reflectors the technique has also been applied to vegetated landslides by Singleton et al. (2014). Crossetto et al. (2012) have applied it to terrestrial SAR in the Ku-band, also tracking artificial corner cube reflectors.

Herein, we focus on tracking natural objects rather than corner cubes, using a terrestrial instrument. There is the additional challenge that the complex signal (amplitude and phase) of Ku-band radar is strongly affected by atmospheric influences accu-

mulating along the LOS of several km through the turbulent atmospheric boundary layer.

Our approach is designed to enable tracking of weakly reflecting natural features over large distances (the application example involves a LOS of up to 6.5 km in alpine environment). It therefore starts with data preparation (sec. 2.1) to make weakly reflecting natural scatterers distinguishable and thus trackable by enhancing their signal-to-noise ratio. Two methods, one working on a local level (sec. 2.2) the other one on a global level (sec. 2.3), are then presented to actually track features in the amplitude images. The methods are then applied to a real data set (sec. 3) representing fast surface changes (downhill displacements of up to 2 m/day) associated with low quality features, i.e. ice patterns on a steep alpine glacier tongue.

The results are then compared to the deformations obtained from phase-based interferometry (sec. 4). The discussion shows that the proposed methods work well for large displacements or longer time spans. They are complementary to the interferometric approach. Their potential to deliver 2D displacement information is another benefit.

2 Radar amplitude feature tracking approaches

Single look complex (SLC) images resulting from TRI are matrices of complex numbers z representing an average phase $\varphi = \arg(z)$ and amplitude $a = |z|$ per pixel corresponding to the superposition of the radar signals reflected by all surfaces within the corresponding azimuth-range cells. For amplitude feature tracking the phase is not required. The images used for further processing are therefore directly obtained from |SLC|. We assume that the images are already registered, e.g. because they were acquired using a sufficiently stable instrument setup.

2.1 Data preprocessing

The amplitude values extracted from an SLC are affected by noise including atmospheric effects (spatially and temporally variable attenuation, especially due to water vapor, vertical refraction) and temporally changing surface properties (e.g. due to moisture). This impairs the signal-to-noise ratio and causes local variations of the amplitude, especially for weakly reflecting surfaces like natural surfaces (as opposed to specially installed artificial radar reflectors). The raw amplitude images received from individual radar acquisitions by the instrument must therefore be prepared to make persistent weakly reflecting natural features on ice and rock surfaces visible and thus trackable in the first place. The preparation consists of the following steps:

1) *Spatial correction:* The attenuation of the amplitude caused by changing atmospheric conditions can exhibit significant local variations. This effect is mitigated by local histogram correction of each amplitude image. For each epoch t, the corresponding image $I_{t,raw}$ is convolved with a Gaussian average filter of size s to obtain an estimate of the local mean I_{t,s_mean} for each pixel (mean of its neighborhood). Similarly the local standard deviation $I_{t,\_std}$ is estimated from the same neighborhood. Afterwards, the image is locally normalized by transforming each pixel according to

$$\bar{I}_t(i,j) = \frac{I_{t,raw}(i,j) - I_{t,s\_mean}(i,j)}{I_{t,s\_std}(i,j)} \qquad (1)$$

where i and j are the pixel indices.

2) *Temporal correction:* Temporal changes of surface properties can cause large temporal variations of the amplitude. Temporal low pass filtering can mitigate this effect. We achieve this by averaging $n+1$ locally corrected amplitude images:

$$I_{t,\mathrm{avg}}(i,j) = \frac{1}{n+1} \sum_{r=-n/2}^{n/2} \bar{I}_{t+r}(i,j) \qquad (2)$$

3) *Contrast enhancement:* The probability density function (PDF) of the amplitudes within an SLC-image is that of a Rayleigh-distribution (Hanssen, 2012). This is suboptimal if the focus for tracking lies on natural features that are not very pronounced. Thus, the contrast among targets having weak reflectance is enhanced by applying a logarithmic transformation to the raw amplitudes:

$$I_{t,\log}(i,j) = \ln\left(I_{t,\mathrm{avg}}(i,j) - \min_{t,i,j}(I_{t,\mathrm{avg}}(i,j)) + 1 \right) \qquad (3)$$

where the constant offset of 1 ensures that the resulting distribution is closer to a normal dis-

tribution. Finally, the transformed amplitudes are rescaled such that they lie within [0, 1]:

$$I_{t,\mathrm{norm}}(i,j) = \frac{I_{t,\log}(i,j)}{\max_{t,i,j}(I_{t,\log}(i,j))} \quad (4)$$

4) *Interpolation to a regular metric grid*: If the subsequently used tracking technique requires an isotropic and homogeneous pixel grid on the monitored surfaces (e.g. a quadratic Cartesian grid) resampling of the temporally corrected, normalized amplitude images from azimuth-range bins to a homogeneous grid is carried out by using cubic interpolation.

Once all preprocessing steps have been accomplished, the amplitude images $I_t(x,y)$ of the individual epochs t are available for feature detection and tracking.

2.2 Least squares template matching

Image correlation used for tracking of multiple features in an image sequence works locally and must therefore be performed separately for each feature. A matching template in frame t is selected symmetrically around a feature and the correspondence is searched using the reference template within frame $t+1$.

Initially, features must be detected in the radar amplitude image sequences. The appearance of natural or artificial scatterers in the images suggests using a blob detection approach. The *difference of Gaussians* (DoG) operator (Szeliski, 2010) is well suited as it favors features having distinct gradients in all directions. Furthermore, DoG allows scale invariant feature detection by searching for scale-space extrema. To suppress particularly weak targets, a threshold θ_1 (see Appendix A) on the local maximum detection was applied. A spatial filter of size θ_2 that favors large amplitude features was then applied to remove closely positioned extrema and create an approximately homogeneous feature distribution.

Least squares template matching (Grün, 1985; Bethmann et al., 2011) is a sub-pixel accurate technique that iteratively solves the correspondence problem. The changes between the reference and the matching template must be small. If they are not necessarily so, they need to be determined approximately beforehand, e.g. using cross-correlation, and reduced by an appropriate prior transformation, e.g. translation. LSM has the advantage that the functional model is easily adaptable to various problems. In particular, radiometric as well as geometric parameters can be estimated allowing for changes in grey levels (amplitudes) and for shape changing templates. The model used herein is given by the observation equation

$$I_{t+1}(x,y) + v_{t+1}(x,y) = r_0 + r_1 \cdot I_t\left(f_x(x,y), f_y(x,y)\right) \quad (5)$$

with f_x and f_y as geometric transformations, e.g. bivariate polynomials of n^{th} degree. Here, we use an affine transformation (1st order bivariate polynomial) represented by the parameters $\{p_0, p_1, \ldots, p_5\}$ to allow for geometrical changes of the template:

$$f_x(x,y) = x' = p_0 + p_1 x + p_2 y \quad (6a)$$

$$f_y(x,y) = y' = p_3 + p_4 x + p_5 y \quad (6b)$$

To account for systematic radiometric differences between the templates, offset and gain parameters $\{r_0, r_1\}$ are introduced, and all residual deviations are lumped together in the residuals v.

The functional model is nonlinear with respect to the transformation parameters and must therefore be linearized. The linearized image function is given by

$$g_{x',t} = \frac{\partial I_t(x',y')}{\partial x'} \text{ and } g_{y',t} = \frac{\partial I_t(x',y')}{\partial y'}, \quad (7)$$

where the approximations of the grey level gradients $g_{x'}$ and $g_{y'}$ are computed from the matching template by convolution with a normalized Sobel kernel that also includes a smoothing effect in complementary direction. The least squares solution is then obtained by iteratively minimizing the L_2-norm of the residuals v. For each iteration step, the matching template is transformed by the updated parameters and resampled by cubic interpolation which is a practically sufficient approximation to the theoretically optimal sinc interpolation (Dodgson, 1992).

The final transformation parameters are obtained when convergence is reached. The quality of the result is assessed by standard error analysis for least squares adjustment using the global model test, posterior standard deviations and correlations of the estimated parameters. Finally, the translation of the center point of the matching template is calculated to represent the amplitude feature's motion between the two frames.

2.3 Optical flow

A different approach to estimate motion in a radar amplitude image sequence is optical flow, the most general approach to motion estimation in an image sequence. Motion components are calculated for each pixel based on the *grey value constancy assumption* (Szeliski, 2010)

$$I(x,y,t) = I(x+u, y+v, t+1)\,, \tag{8}$$

where u and v are horizontal and vertical optical flow components describing the flow between an image $I(t)$ and $I(t+1)$, the time t is now written as an argument instead of an index, and we assume that the units of time are adjusted such that the time increment between the two images is 1. The linearized form of (8) leads to the *optical flow constraint* as first described by Horn and Schunck (1981):

$$I_x u + I_y v + I_t = 0 \tag{9}$$

Here, I_y and I_x are the derivatives of I with respect to x and y, and I_t is the derivative with respect to time. To measure the global deviation from the *grey level constancy assumption* an energy term based on (8) is introduced with $\mathbf{x} := (x,y,t)^{\mathrm{T}}$ and $\mathbf{w} := (u,v,1)^{\mathrm{T}}$:

$$E_{Data}(u,v) = \int_{\Omega} (|\, I(\mathbf{x}+\mathbf{w}) - I(\mathbf{x})\,|^2)\mathrm{d}\mathbf{x} \tag{10}$$

This is an underdetermined problem and cannot be solved without further constraints since two motion components are estimated for each pixel. Therefore, the assumption that neighboring points move with similar velocity is introduced. This is called *smoothness constraint* and penalizes abrupt changes in the velocity fields u and v:

$$E_{Smooth}(u,v) = \int_{\Omega} (|\,\nabla u\,|^2 + |\,\nabla v\,|^2)\mathrm{d}\mathbf{x} \tag{11}$$

The combination of E_{Data} and E_{Smooth} leads to the total error E:

$$E(u,v) = E_{Data} + \alpha E_{Smooth} \tag{12}$$

where the compromise between constant grey levels and a smooth velocity field is controlled by the regularization parameter $\alpha > 0$ (Nixon et al., 2012; Brox et al., 2004). The final objective function is obtained by formally replacing the squared norm by a more general function $\psi(\cdot)$ (which can but does not need to be $|\cdot|^2$):

$$E(u,v) = \int \psi(|\, I(\mathbf{x}+\mathbf{w}) - I(\mathbf{x})\,|^2) + \alpha\psi(|\,\nabla u\,|^2 + |\,\nabla v\,|^2)\mathrm{d}\mathbf{x} \tag{13}$$

The optical flow code used in this paper is taken from Liu (2009). The implemented approach is based on Brox et al. (2004) and Bruhn et al. (2005). It combines local and global optical flow allowing for discontinuities in the flow field. Moreover, a multi-scale approach using a Gaussian pyramid is used to prevent the algorithm from getting stuck in a local minimum.

The quality of the flow field strongly depends on the choice of α. A low value may result in an overfit whereas a high value may lead to oversmoothing. The optimal prediction principle (OPP) is a concept introduced by Zimmer et al. (2011) for overcoming this problem and selecting α automatically. It is based on the assumption that the flow field is also smooth in time. Choosing α too small or too large leads in this case to a bad prediction of future frames using the estimated field. The parameter α is therefore chosen such that the frame I_2 is predicted most precisely by the flow field estimated from the frames I_0 and I_1. The frame batch I_0, I_1 and I_2 must be equidistant in time but can start at any epoch. Raket (2012) formulated the OPP more generally for any frame k in which

$$P_k(\alpha) = \int_{\Omega} |\, I_k(\mathbf{x} + k\mathbf{w}_{\alpha}(\mathbf{x})) - I_0(\mathbf{x})\,|\,\mathrm{d}\mathbf{x} \tag{14}$$

is minimized for some k. Here, the case $k = 2$ is evaluated for a flow field $\mathbf{w}$ estimated between the frames I_0 and I_1. This is conducted for a large set of α values, the one that best describes the flow field in I_2 is chosen. This procedure for determining an optimum value of alpha is computationally intensive and is therefore ideally conducted only once for a scene whose flow behavior does not change significantly over the monitoring period. Naturally, a reference flow field can always be used as an alternative to OPP if available.

3 Application example

The above methods are now applied to a monitoring example where natural features on ice, snow and rock are tracked. The latter are stable thus allowing to check the results for plausibility.

3.1 Project

The Bisglacier (Switzerland) has a steep tongue which is 1.5 km long and starts with a scarp (Fig. 1, red box) where movements of up to 2 m/day are expected. During summer 2014 it was monitored from a distance of up to 6.5 km using a GPRI terrestrial radar interferometer set up on the opposite slope. The instrument operates in the Ku-band, has a range resolution of 0.75 m and an azimuth resolution of 0.4 deg given by the real aperture. Its minimum bin width in azimuth direction is 0.1 deg due to the step width of the azimuthal scanner (Werner et al., 2008). In order to reduce potential loss of coherence due to the turbulent atmosphere and large deformation rates data were acquired at a rate of 2 min. Further details and interferometric processing results are given in Butt et al. (2016).

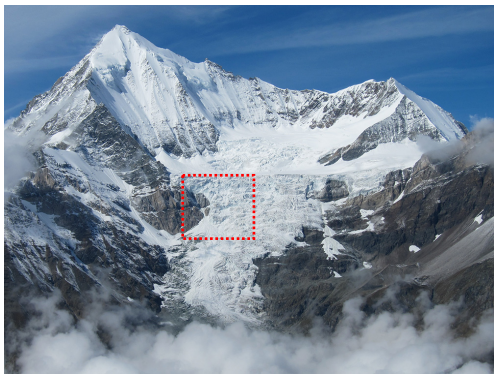

Fig. 1 Bisglacier, seen from GPRI location at opposite slope.

3.2 Tracking of amplitude features

The highly variable atmospheric conditions over the long line of sight are a significant challenge for interferometric processing of the phase but they also affect the amplitude. Ferretti et al. (2001) introduced the amplitude dispersion index (ADI) for measuring the relative variation of the amplitude. It is obtained as the ratio of amplitude standard deviation σ_a to mean m_a over a certain time. The ADI is typically used to identify high quality scatterers (ADI < 0.25) within a set of radar images for persistent scatterer interferometry, see e.g. Kampes (2006). However, the ADI also indicates the quality of amplitude features. In our example, the rock surfaces surrounding the glacier have a mean ADI of 0.3, the ice and snow covered surfaces have a mean ADI of 0.5. So, the temporal variation of the amplitudes is high for these natural scatterers and preprocessing (sec. 2.1) helps to raise natural features sufficiently above noise level in the first place.

Atmospheric effects are not the only reason for a large ADI. As described by Willatt et al. (2010), the penetration of Ku-band waves into snow and ice and thus the amplitude of the reflected waves depends on the wetness of the material. This means that we expect diurnal patterns for the glacier considering that incident sunlight increases the wetness near the surface during the day whereas falling temperatures cause refreezing during the night. More generally, varying material properties will cause amplitude variations and thus higher ADI.

A third issue is the fact that a glacier behaves like a highly viscous, incompressible, flowing fluid (Jouvet et al., 2011). This means that the trackable features change shape over time. It will depend on the adaptivity of the tracking method and on the chosen parameters to which extent this affects the quality of the results.

Data Preparation

The radar instrument is set up on a pillar and its orientation is sufficiently stable. So, no registration or geometric transformation of the individual radar images is required. The raw amplitude data are preprocessed according to the steps described in sec. 2.1. The specific parameters used are summarized in table A.1 in the appendix. The temporal low pass filtering (step 2) consisted in calculating daily averages such that also the variations due to material property changes were largely mitigated.

Least Squares Template Matching

In accordance with sec. 2.2, the DoG approach was used to detect blob like features for tracking. The blob detection was applied to only one daily average amplitude image (August 01, 2014). This image was subsequently used as starting frame associated with epoch t_0. The centers of the detected blobs are indicated by the black circles in Fig. 2 which shows the part of the amplitude image corresponding to the previously mentioned scarp section (red box in Fig. 1).

The reference templates were selected symmetrically around the blob centers in frame t_0. Their size was chosen such that they are approximately quadratic with a side length of 50 m in a metric system. This small template size is a compromise between matching accuracy and resolution i.e., density of tracked features on the glacier. The matching templates were selected symmetrically about the same

coordinates, but larger. To cope with fast changes of the shape of the features a time difference of only $\Delta t = 1$ day was chosen between the reference and the matching templates. After each matching, the templates were updated by selecting the pixels within the respectively shifted symmetric region. The coordinates of the tracked features within the radar images were also updated after each matching step by adding the accumulated displacements since t_0 to the initial pixel coordinates.

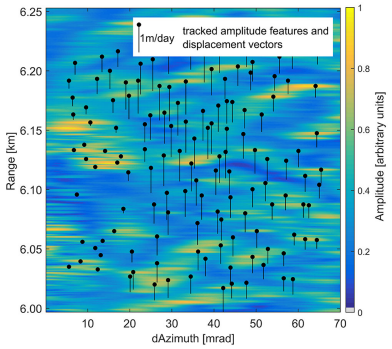

Fig. 2 Amplitude image of 08/01/2014 (after preprocessing); area covered corresponds to red box in Fig. 1

In our particular example the geometric transformation (6ab) can be simplified to just a translation because no rotation or shear is expected for features on the glacier, at least not within the time steps of one day. To ensure a good quality of the match, we have implemented several ad hoc solutions to detect adjustments that do not converge. In such cases, the model is further reduced, and it is rejected entirely if the posterior variance factor σ_0^2 exceeds a threshold θ_3. In our current software the previous path of motion is extrapolated for the current time interval in case of model rejection.

The features that were detected in frame t_0 are tracked throughout the image sequence. Although the reference template is adapted after each time step Δt errors will occur if features disappear or newly appear after a while. To avoid this problem, a future extension of the LSM tracking should include a feature update process which terminates tracking of vanished features (e.g. based on the matching quality metrics mentioned in the previous paragraph) and initiates tracking of newly appeared ones (e.g. based on a DoG-based blob detection like for the starting frame).

The results of LSM-based tracking for a period of 30 days are visualized in Figs. 2 and 3 (left), and discussed in sec. 3.3.

Optical Flow

For optical flow the interpolation to a metric grid (sec. 2.1, preparation step 4) is necessary because the smoothness (11) of the flow fields is evaluated isotropically within u and v while the radar images have different resolution in azimuth and range direction.

The following OF computations were carried out using the C++ program from Liu (2009). Again, the chosen parameters of the algorithm are summarized in table A.1 in the appendix. Most of them, except the regularization parameter α, were chosen by trial and error without an in-depth analysis (which is left for future work). As a result of the data driven OPP (sec. 2.3), α depends on the magnitude of the displacements and on the noise level, and thus indirectly on the time interval Δt. In our example, the amplitude (grey level) noise within actually stable areas was found to be around twice as large as the mean absolute grey level differences in areas with significant glacier surface motion for $\Delta t = 1$ day. To reduce the influence of noise on the OPP result, different temporal baselines $\Delta t \geq 4$ days were chosen. In these cases the above ratio became 1 or much better. However, as stated in 2.3, α can also be determined using a reference field. Indeed we have used the interferometric displacement field for this purpose ignoring the fact that the accumulated interferometric displacements do not represent exactly the same changes as observed through the amplitudes

For the result presented in section 3.3 a temporal baseline of $\Delta t = 30$ days has been used. The optimum regularization parameter was found to be $\alpha = 0.025$ for this case. The flow field in range direction was converted from pixels to m/day using Δt and the range resolution of 0.75 m. The flow field in azimuth direction evaluated for OF was converted by calculating the range dependent bin resolution in azimuth direction.

3.3 Results

Fig. 3 shows the results of LSM-based feature tracking (left) along with the ones obtained by interferometry (right). The corresponding result of optical flow can be seen in Fig. 4a. All these results cover the same 30-day period from August 1 to August 31, 2014.

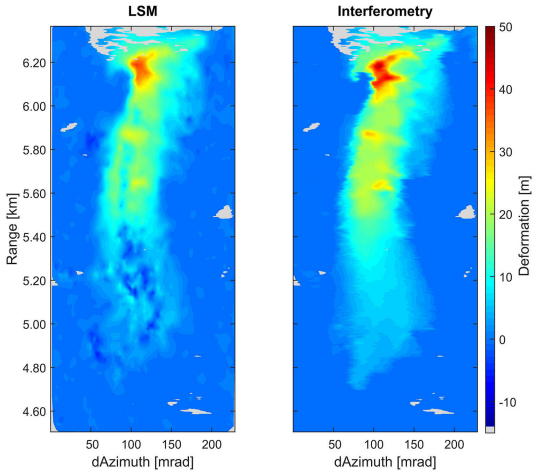

Fig. 3 Results of feature tracking using LSM (left) and of interferometric phase accumulation (right); gray color represents areas excluded due to exceptionally low coherence.

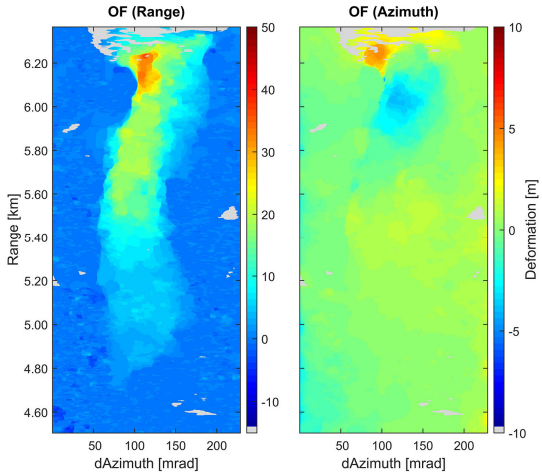

Fig. 4 Results of feature tracking using OF showing displacements in range (left) and in azimuth direction (right).

The steep scarp indicated by the red box in Fig. 1 can be recognized in Fig. 3a/b and Fig. 4a as the area with the largest displacements. The results are here depicted in radar coordinates. So, the image is metrically distorted. In reality it covers a width of 1 km at the bottom (surface at a distance of 4.50 km from the radar instrument), a height of 1.85 km and a width of 1.50 km at the top (surface at a distance of 6.4 km). The figure shows the total displacement observed during the 30 days. For the two feature tracking methods it displays the range-component of the displacement of features. The feature tracking methods are theoretically capable of also tracking azimuthal displacements. However, only the result of OF revealed a significant displacement in azimuth direction which is shown in Fig. 4b.

For LSM, daily coordinates were obtained for about 3900 features (see Fig. 5). The continuous deformation field shown in Fig. 3a was obtained by cubic interpolation between the tracked points. Optical flow directly yields a continuous displacement field. However, only the daily averaged amplitude images from the first and last day were used for OF. This large temporal baseline demonstrates the capability of OF to even bridge a large data gap. It has to be considered that the features tracked on a day-by-day basis using LSM have significantly changed shape and appearance between the two frames used for OF. The larger structures, however, obviously remain sufficiently similar to determine the flow components.

Figure 3b shows the total surface displacement within each azimuth-range bin as obtained by interferometry. Unwrapped 2 minute interferograms were initially summed up over 2h. The resulting temporally low pass filtered interferograms were then corrected by subtracting the atmospheric phase screen observed on stable points (ADI < 0.2) and interpolated by natural neighbor interpolation over the area of the glacier. Subsequently, the corrected 2-hour interferograms were stacked from midday of 8/1/2014 until midday of 8/31/2014.

Even though Fig. 3a/b and 4a show deformation in line-of-sight direction, they are not supposed to be exactly identical because the accumulated surface changes within azimuth-range bins will typically differ from the displacement of surface structures visualized in terms of azimuth and range. The comparison will be continued in sec. 4.2.

4 Discussion

4.1 Comparison of LSM and OF

The methods presented above have very different characteristics. Least squares template matching tracks individual, distinct features relying on their respective local neighborhood. The matching interval must balance between a time interval long enough for sufficient signal-to-noise ratio (see sec. 2.1) and short enough such that potential shape changes of the feature over time can be accommodated. The result over a longer time span is a trajec-

tory within the azimuth-range space for each of these features, see Fig. 5. To obtain an areal picture (Fig. 3) a continuous flow field must be interpolated between the features actually tracked. The LSM algorithm is computationally intensive since it must be iterated separately for each feature and matching time-step. On the other hand it is well suited for parallelization, and given the individual trajectories it allows in-depth analysis of displacement patterns.

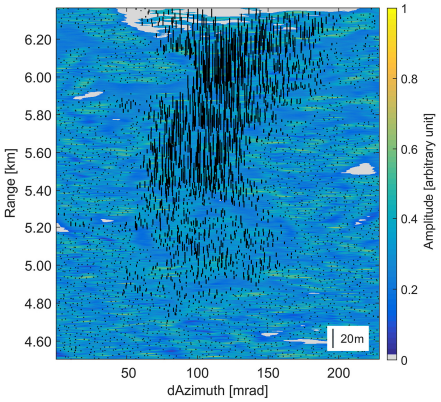

Fig. 5 Displacements in range direction for features tracked by LSM

Optical flow on the other hand is a more global method depending on the degree of low-pass filtering enforced by the chosen value of α. This is an advantage in terms of stability and a disadvantage in terms of resolution. The results depend much less on the behavior of single pixels and take also less dominant structures into account if they are large enough. So, OF can bridge areas with weak texture or larger noise levels and time spans during which individual features may change considerably. On the other hand, the deformations of small structures (a few pixels only) and local changes of the flow field may remain undetected.

In our example both methods led to remarkable results considering that deformations of a glacier could be estimated by using only radar amplitude information of natural features with especially weak and highly varying reflectance, observed from a distance of up to 6.5 km. However, both methods also showed weaknesses in this particular example.

Crossetto et al. (2012) showed that the potential accuracy is 1/85 of a pixel when tracking corner cube reflectors. The lower the temporal variation of the amplitudes and the smaller the change of geometry within a template the more accurate the LSM result gets. In our case, LSM suffered from the fact that the tracked features (structure of the ice surface) were weak and changed shape over time, and that our algorithm did not include special handling of vanishing and newly appearing features. A particular example of these effects are the vertical stripes at ranges between 4.8 and 5.8 km in Fig. 3a. The top ones perfectly coincide with the line of falling ice originating from the scarp above. The lines below coincide with a flat part at the end of the glacier, where we have a mixture of ice and rock debris, low-texture snow fields, and additionally very flat angle of incidence of the LOS. The quality of the result can most likely be increased significantly, by improved data preprocessing, proper feature update, advanced error handling, and introduction of a stochastic model into the matching process.

Optical flow in comparison had the tendency to deliver patchy flow fields showing small but systematic deviations from the true flow. This effect is related to the combination of local and global optical flow and strongly depends on the regularization parameter. We found that the numeric value of α obtained by OPP depends significantly on the image section, time interval and dates of the images used. We attribute this to the low, time-dependent signal-to-noise ratio and to local variations of the flow field dynamics. OF based on a locally adaptive regularization parameter could help mitigating this problem. Additionally, as with LSM, it may be beneficial to further investigate the impact and appropriate choice of the matching time interval.

4.2 Comparison with interferometry

Different observation types

Despite the fact that both approaches, amplitude feature tracking and interferometry, provide information on changes in line-of-sight direction, the reference of the observed changes and thus their interpretation is totally different.

TRI yields phase differences Δφ between two acquisitions discretized in range and azimuth bins (pixels within the radar images). Having a continuous time series of Δφ values per pixel, they can be summed up to obtain the total deformation per pixel. For each pixel, this deformation then represents the weighted mean of the displacement of all scatterers within the corresponding azimuth-range bin during the time covered by the radar images. Given the bin width in range direction (0.75 m) and the time scale of the changes (up to 2 m/day in our example), it

may take several hundred interferometric acquisitions until an object passes through one bin. The individual phase differences and therefore also the accumulated deformations are not only affected by displacements or deformation within the bin but also by material moving into the bin or out of it. Processes like the constant breakoff of small pieces of material (stones, ice, etc.) in areas with high motion dynamics may lead to a systematic overestimation of LOS deformations. A similar effect but with opposite sign occurs with melting snow. Breakoff of a large ice mass will cause loss of coherence in the respective bins for a short period of time, interrupting the displacement time series. The accumulated interferometric phase shifts will therefore not represent how much the corresponding surface has actually moved towards the radar interferometer or away from it, but it will rather represent the average LOS velocity of the dominant reflectors within the respective bin.

Feature tracking, on the other hand, yields estimates of displacements of actual objects or surface elements parameterized in range and azimuth direction. Low-pass filtering is involved through the smoothness constraint with OF and through the template size and spatial interpolation with LSM. Furthermore, just like in the case of interferometry, physically disjoint surface patches may be mapped into a single azimuth-range bin (thus mixing features) if the surface topography and the location of the instrument cause equal ranges to be obtained for surfaces at different altitude. This means that the trajectories resulting from feature tracking may underestimate the actual motion of individual (small) objects moving at higher speed than their neighborhood whereas they will accurately represent the motion of contiguously moving surface areas.

Accuracy

Interferometry is well suited for very accurate measurement (mm level) of quasi-instantaneous deformation rates i.e., average LOS displacements within short time intervals (a few hours, possibly less). This is particularly useful for monitoring stability or constancy of motion, and for quickly detecting accelerations. Amplitude feature tracking of natural surfaces is not able to provide such information with comparable accuracy, and would be useful for monitoring constancy of motion only with very large displacement rates where interferometry might fail due to loss of coherence (rare case). Reasonable accuracies for feature tracking can be expected for larger time intervals (e.g. days or longer) or with many particularly strong reflectors within the monitored area. It may be a useful complement or alternative to TRI if the latter suffers from poor coherence (e.g. due to debris or vegetation) or if monitoring needs to be continued after a long break (days, weeks or months) and feature tracking helps assessing changes that occurred during the break.

A rough estimation of the achieved accuracies for all methods is done by comparing the results to the expected deformation of 0 m for the known, stable areas (solid rock) surrounding the glacier. There, the median absolute deviation (MAD) of the calculated displacements over the entire 30-day period is 1.5 cm for interferometry, 20.0 cm for optical flow and 9.0 cm for LSM. While interferometry seems clearly better here, it needs to be considered that the atmospheric corrections used for the interferometric processing were obtained from the stable areas assuming that they are stable. No such constraint was used for feature tracking.

Lacking independent measurements (e.g. using GNSS) we could not quantify the accuracy achieved in the moving areas. We assume that it is slightly worse than in the stable ones because of the above effects, and in case of interferometry also the interpolation of the atmospheric corrections. The median deviation between the TRI and OF results amounts to -74 cm within the moving area, and -118 cm between TRI and LSM. So, feature tracking indicates significantly less total displacement over the 30 days than interferometry. The likely reasons have been discussed above. The smaller average displacements indicated by LSM are very likely associated with the masking of trackable features by debris and breakoffs and to the lack of trackable features in some areas, to which LSM is more sensitive than OF, as discussed in sec. 4.1. Further investigations are needed to clarify this.

2D capability

Radar amplitude feature tracking can deliver displacement information in range and in azimuth direction. It is thus an approach yielding 2D information with a single instrument, as opposed to interferometry which yields displacements in range direction only. However, the azimuth component will typically be much less accurate than the range com-

ponent, and thus sensitivity in azimuth will be much worse than in range. This is due to the fact that the fixed azimuth-range bins of e.g., 4 mrad by 0.75 m translate into metric spatial bins whose width depends on the distance. In our case, these bins correspond e.g. to 20 m by 0.75 m for surfaces at a distance of 5 km. So, the accuracy of the azimuth component of the estimated displacements will be worse by a factor of about 30. Nevertheless, the 2D capability of amplitude feature tracking can still deliver very valuable information for the interpretation of the monitoring data.

5 Conclusion

We have presented two methods for amplitude-based feature tracking of natural surfaces within terrestrial radar data: least squares template matching (LSM), and optical flow (OF). A proposed preprocessing of the radar data improves the signal-to-noise ratio and makes the features trackable despite significant fluctuations of atmospheric attenuation and surface reflectivity. We have tested the resulting algorithms using 30 days of radar data originally obtained for interferometric glacier monitoring from a distance of 4.5 to 6.5 km.

The analysis showed that the line-of-sight displacement components over the entire 30 days period were obtained with a MAD of about 20 cm using OF and about 9 cm using LSM within actually stable areas. The accuracy within the moving areas could not be assessed quantitatively because of lacking ground truth data. Comparing to the interferometric results and the approximately known dynamics of the monitored glacier, we expect that the results are only slightly less accurate for those areas. LSM has the advantage of delivering pointwise results in the sense of displacement trajectories of individual features. When needed, these results can be interpolated to obtain a spatially continuous displacement field. The accuracy is mainly limited by the strength of the signals reflected from the observed scatterers, and the potential of LSM was therefore not fully exploited within the present application where the tracked natural features (inhomogeneities of the ice surface) were weak compared to the noise level of the data.

OF is suitable for truly areal monitoring because it directly yields a smooth displacement field. It is therefore better suited for deformation estimation in areas with little texture but cannot directly expose discontinuities of the displacement field. The application example demonstrated that OF works very well for long time intervals between the images and its spatial smoothing mitigates the impact of slight shape changes of individual features.

Both methods provide valuable complementary information to interferometry. Representing actual surface motion instead of accumulated LOS-velocities they can support the interpretation of interferometric results. They can bridge spatial and temporal data gaps resulting from ambiguity problems and loss of coherence with interferometry. Finally, they provide an additional displacement component in azimuth direction that allows quantifying actual 2D displacements, although much less accurately than in range direction (factor of 30, in our example).

Several ideas for improvements of the algorithms and for required further investigations have been given. We expect that they will enable applicability of amplitude feature tracking to a variety of real-world monitoring problems.

Acknowledgement

Prof. Martin Truffer, University of Alaska, has provided the GPRI instrument. The data were collected in cooperation with Prof. Martin Funk, ETH Zürich. The Swiss Federal Office for the Environment has supported the data collection financially.

References

Bethmann, F., and T. Luhmann (2011). Least-Squares Matching with Advanced Geometric Transformation Models. *Photogrammetrie - Fernerkundung - Geoinformation*, No. 2, pp. 57-69.

Bhattacharya, A., K. Mukherjee, M. Kuri, M. Vöge, M. L. Sharma, M. K. Arora and R. K. Bhasin (2015). Potential of SAR Intensity Tracking Technique to Estimate Displacement Rate in a Landslide-Prone Area in Haridwar Region, India. *Natural Hazards*, Vol. 79, No. 3, pp. 2101-2121.

Brox, T., A. Bruhn, N. Papenberg and J. Weickert (2004). High Accuracy Optical Flow Estimation Based on a Theory for Warping. In: *Proc. of 8th European Conference on Computer Vision*, Vol. 4, Springer-Verlag Berlin, pp. 25-36.

Bruhn, A., J. Weickert and C. Schörr (2005). Lucas/Kanade Meets Horn/Schunck: Combining Local and Global Optic Flow Methods. *International Journal of Computer Vision,* Vol. 61, No. 3, pp. 211-231.

Butt, J., S. Conzett, M. Funk and A. Wieser (2016). Terrestrial Radar Interferometry for Monitoring Dangerous Alpine Glaciers: Challenges and Solutions. In: *Proc. of GeoMonitoring*, Braunschweig, Germany.

Crosetto, M., O. Monserrat, G. Luzi and N. Devanthéry (2013). A Noninterferometric Procedure for Deformation

Measurement Using GB-SAR Imagery. *IEEE Geoscienec and Remote Sensing Letters*, Vol. 11, No. 1, pp. 34-38.

Dodgson, N. A. (1992). Image Resampling. Technical Report. Dept. Computer Laboratory, University of Cambridge, pp. 117-122.

Ferretti, A., C. Prati and F. Rocca (2001). Permanent Scatters in SAR Interferometry. *IEEE Transactions on Geoscience and Remote Sensing*, Vol. 39, No. 1, pp. 8-20.

Gruen, A. W. (1985). Adaptive Least Squares Correlation: A Powerful Image Matching Technique. *South African Journal of Photogrammetry, Remote Sensing and Cartography*, Vol. 14, No. 3, pp. 175-187.

Hanssen, R. F. (2002). Radar Interferometry, Data Interpretation and Error Analysis. Vol. 2, Kluwer Academic Publishers New York, Boston, Dordrecht, London, Moscow, pp. 80-159.

Horn, B. K. P., and B. G. Schunck (1980). Determining Optical Flow. *Artificial Intelligence*, Vol. 17, pp. 185-203.

Jouvet, G., M. Picasso, J. Rappaz, M. Huss and M. Funk (2011). Modelling and Numerical Simulation of the Dynamics of Glaciers Including Local Damage Effects. *Mathematical Modelling of Natural Phenomena*, Vol. 6, No. 5, pp. 263-280.

Kampes, B. M. (2006). Radar Interferometry, Persistent Scatterer Technique. Vol. 12, Springer Netherlands, pp. 5-30.

Liu, Ce. (2009). Beyond Pixels: Exploring New Representations and Applications for Motion Analysis. Ph.D. Thesis, Dept. of Electrical Engineering and Computer Science, Massachusetts Institute of Technology.

Nixon, M. S., and A. S. Aguado (2012). Low-Level Feature Extraction (including Edge Detection). *Feature Extraction & Image Processing for Computer Vision*. Third Edit, Elsevier Ltd, pp. 204-212.

Rakêt, L. L., (2012). Local Smoothness for Global Optical Flow. In: *Proc. of International Conference on Image Processing (ICIP), 19th IEEE*, IEEE, Orlando FL, pp. 57-60.

Singleton, A., Z. Li, T. Hoey and J. P. Muller (2014). Evaluating Sub-Pixel Offset Techniques as an Alternative to D-InSAR for Monitoring Episodic Landslide Movements in Vegetated Terrain. *Remote Sensing of Environment*, Vol. 147, pp. 133-144.

Strozzi, T., A. Luckman, T. Murray, U. Wegmüller and C. L. Werner (2002). Glacier Motion Estimation Using SAR Offset-Tracking Procedures. *IEEE Transactions on Geoscience and Remote Sensing*, Vol. 40, No. 11, pp. 2384-2391.

Szeliski, R. (2010). Computer Vision: Algorithms and Applications. Draft, Springer, pp. 381-426.

Werner, C., T. Strozzi, A. Wiesmann and U. Wegmüller (2008). Gamma's Portable Radar Interferometer. In: *Proc. of 13th FIG Symposium on Deformation Measurement and Analysis*, Lisbon.

Willatt, R. C., K. A. Giles, S. W. Laxon, L. Stone-Drake and A. P. Worby (2010). Field Investigations of Ku-Band Radar Penetration into Snow Cover on Antarctic Sea Ice. *IEEE Transactions on Geoscience and Remote Sensing*, Vol. 48, No. 1, pp. 365-372.

Zimmer, H., A. Bruhn and J. Weickert (2011). Optic Flow in Harmony. *International Journal of Computer Vision*, Vol. 93, No. 3, pp. 368-388.

Appendix A

Table A.1. Summary of parameters used for the numerical results in this paper; reference column (Ref.) indicates in which section the parameter is discussed; parameters marked with an asterisk have been chosen ad-hoc without an investigation or formal optimization, they are only mentioned in the respective sections of the paper.

Sign	Parameter description	Value	Ref.	Comment
n	number of epochs for temporal averaging	720	2.1*	2min apart (720 SLCs correspond to 1 day)
s	window size of local averaging filter	200 m	2.1*	Gaussian filter with 60 m std. in range and azimuth direction
s_R	LSM reference template size	[5, 61]	3.2*	size in azimuth and range direction for bins with a resolution of [0.1 deg, 0.75 m]
s_M	LSM matching template size	[7, 71]	3.2*	size in azimuth and range direction
σ_{DoG}	filter size	1.6	3.2	for start σ, next is factor 1.6 larger
θ_1	response threshold	0.27	2.2*	suppresses weak targets after DoG
θ_2	spatial threshold for features	[3, 31]	2.2*	in azimuth and range direction
θ_3	accuracy threshold (σ_0)	0.055	3.2	to reject a bad LSM match
-	max. LSM iterations	20	2.2	until model is altered
-	upsampling, interpolation	0.75 m, cubic	2.3	for regular metric grid
α_1	regularization parameter	0.053	3.2	Δt=1day, evaluated by OPP
α_2	regularization parameter	0.052	3.2	Δt=4days, evaluated by OPP
α_3	regularization parameter	0.025	3.2	Δt=30days, reference by interferometry
r_G	down-sampling ratio	0.8	2.3*	Gaussian pyramid factor for OF algorithm
-	SOR iterations	30	3.2*	for OF algorithm
-	inner FP iterations	1	3.2*	for OF algorithm
-	outer FP iterations	7	3.2*	for OF algorithm